Oxygen controls on magmatism in rocky exoplanets

Yanhao Lin[a,1], Wim van Westrenen[a,b], and Ho-Kwang Mao[a,1]

[a]Center for High Pressure Science and Technology Advanced Research, Beijing 100094, People's Republic of China; and [b]Department of Earth Sciences, Faculty of Science, Vrije Universiteit Amsterdam, 1081 HV Amsterdam, The Netherlands

Contributed by Ho-Kwang Mao, September 22, 2021 (sent for review June 5, 2021; reviewed by Abby Kavner and Yigang Xu)

Refractory oxygen bound to cations is a key component of the interior of rocky exoplanets. Its abundance controls planetary properties including metallic core fraction, core composition, and mantle and crust mineralogy. Interior oxygen abundance, quantified with the oxygen fugacity (fO_2), also determines the speciation of volatile species during planetary outgassing, affecting the composition of the atmosphere. Although melting drives planetary differentiation into core, mantle, crust, and atmosphere, the effect of fO_2 on rock melting has not been studied directly to date, with prior efforts focusing on fO_2-induced changes in the valence ratio of transition metals (particularly iron) in minerals and magma. Here, melting experiments were performed using a synthetic iron-free basalt at oxygen levels representing reducing (log $fO_2 = -11.5$ and -7) and oxidizing (log $fO_2 = -0.7$) interior conditions observed in our solar system. Results show that the liquidus of iron-free basalt at a pressure of 1 atm is lowered by 105 ± 10 °C over an 11 log fO_2 units increase in oxygen abundance. This effect is comparable in size to the well-known enhanced melting of rocks by the addition of H_2O or CO_2. This implies that refractory oxygen abundance can directly control exoplanetary differentiation dynamics by affecting the conditions under which magmatism occurs, even in the absence of iron or volatiles. Exoplanets with a high refractory oxygen abundance exhibit more extensive and longer duration magmatic activity, leading to more efficient and more massive volcanic outgassing of more oxidized gas species than comparable exoplanets with a lower rock fO_2.

magmatism | oxygen fugacity | Fe-free basalt | high-temperature experiments

Oxygen (~21% in Earth's atmosphere) is essential to life on Earth, and is the most abundant element in the rocky outer layers of Earth (1) as well as the other terrestrial planets in our solar system (2–4). Oxygen can be both refractory (bonded to cations—predominantly Si, Mg, Fe, and Ca—in minerals condensing from planetary disks orbiting young stars) and volatile (condensing in ices—for example, H_2O, CO, CO_2—in the colder outer disk parts) (e.g., ref. 5). The abundance and activity of refractory oxygen in a rock is described using the oxygen fugacity (fO_2), commonly quantified relative to mineral redox buffers, for example, the IW (iron–wüstite) or MH (magnetite–hematite) buffer (6).

The fO_2 conditions in planetary interiors affect the prevailing redox state of polyvalent cations, particularly transition metals (e.g., Fe^0 versus Fe^{2+} versus Fe^{3+}; Eu^{2+} versus Eu^{3+}; Cr^{2+} versus Cr^{3+}) (e.g., ref. 7). The oxygen fugacity in the rocky mantles of the terrestrial planets varies widely. Mercury's rocky outer shell is oxygen depleted, with an fO_2 around 5 log units below that of the iron–wüstite buffer (ρIW−5) (8). As a result, the iron content of Mercury's mantle and crust is very low, with almost all Fe present at Fe^0 in the core. In contrast, Earth's upper mantle today is estimated to contain oxygen levels corresponding to fO_2 of ~ρIW+3 (6), and parts of the Martian mantle may exhibit fO_2 up to ρIW+5 (e.g., ref. 9), yielding mantles with FeO abundances of 8 wt.% and 18 wt.%, respectively.

These current mantle fO_2 values do not necessarily reflect oxygen fugacity conditions during planetary accretion. Mantle oxygen fugacities can change significantly during planetary growth, differentiation, and subsequent evolution. For example, models of accretion and metallic core segregation in Earth (e.g., refs. 10 and 11), based on the observed abundances of siderophile (iron-loving) elements in their mantle, suggest initial fO_2 values during accretion that are Mercury-like, up to 8 log fO_2 units lower than present-day mantle estimates. This suggests significant terrestrial mantle oxidation occurred after the main phase of accretion and core formation, perhaps resulting from late accretion of oxidizing agents such as H_2O (11). Alternatively, in Earth, mantle self-oxidation is proposed to have occurred through the disproportionation reaction $3Fe^{2+}O = Fe_2^{3+}O_3 + Fe^0$ which can take place in the presence of the high-pressure mineral bridgmanite (e.g., ref. 12) or in a deep magma ocean setting (13). If iron metal can be sequestered to the core, this reaction can increase the redox state of the mantle. In Mars and the Moon, lower interior pressures prevented this process, although the increasing stability of Fe^{3+} over Fe^{2+} with increasing pressure (e.g., ref. 14) could still have resulted in significant vertical oxygen fugacity gradients in their magma oceans.

Astronomical observations suggest that both the initial and present-day spreads in terrestrial planet oxygen abundances, masses, and sizes in our solar system are not unusually broad. Many rocky exoplanets have been characterized over the past decade, some with masses and radii far exceeding those of the rocky bodies in our own solar system (e.g., ref. 15). Such planets likely include super-Earths (with compositions perhaps similar to terrestrial planets in our solar system but with significantly higher mass and radius), but also likely include rocky planets with bulk compositions significantly different from compositions found in our solar system. Examples include rocky exoplanets enriched in elements that typically condense at very high temperatures, such as Ca and Al (16); rocky exoplanets rich in water ("ocean worlds")

Significance

Oxygen is not only crucial for life as we know it but also forms the most abundant element in the outer layers of rocky planets in our own solar system and in exoplanetary systems orbiting other stars. Models for rocky (exo)planets suggest that on the order of 50% of all atoms in their rocky shells are oxygen atoms. Here we provide experimental evidence for a significant effect of planetary oxygen abundance on melting of rocks, showing that higher rock oxygen abundance leads to easier rock melting. This suggests that the extent and vigor of magmatism differ greatly between low-oxygen and high-oxygen exoplanets, opening an avenue to couple future observations of exoplanet atmospheres to interior compositions that cannot be directly observed.

Author contributions: Y.L. and W.v.W. designed research; Y.L. and W.v.W. performed research; Y.L. and W.v.W. analyzed data; and Y.L., W.v.W., and H.-K.M. wrote the paper.

Reviewers: A.K., University of California, Los Angeles; and Y.X., Guangzhou Institute of Geochemistry.

The authors declare no competing interest.

[1]To whom correspondence may be addressed. Email: yanhao.lin@hpstar.ac.cn or maohk@hpstar.ac.cn.

This article contains supporting information online at http://www.pnas.org/lookup/suppl/doi:10.1073/pnas.2110427118/-/DCSupplemental.

Published November 1, 2021.

(17); planets that lack a metallic core altogether (18); and planets with high or low C/O ratios (16, 19, 20). The mantle oxygen fugacity in such exoplanets could span a range similar to that found in rocky bodies in our solar system (e.g., refs. 21 and 22).

Effects of fO_2 on Exoplanet Properties

Assessing and quantifying the effects of rock oxygen fugacity variations is important, as fO_2 provides fundamental controls on the first-order interior structure of rocky planets. Refractory oxygen abundance determines the proportion of iron that is reduced to the metallic form, and hence controls the core fraction of terrestrial (exo)planets (5), as well as the mineralogy (23) and viscosity (24) of planetary mantles. The oxygen fugacity of mantle rocks also plays a key role in controlling the speciation of hydrogen- and carbon-bearing species outgassing from early global magma oceans, or from erupting lava during later episodes of volcanic activity (25–28). At high fO_2, volatile species such as H_2O and CO_2 dominate volcanic gas composition, whereas, at low fO_2, the stable species are H_2 and CO, with CH_4 also playing a significant role. As atmospheric gas speciation strongly affects prebiotic chemosynthesis (29), rock oxygen fugacity can therefore also influence a rocky planet's surface habitability.

Magma Oceans on Rocky Exoplanets

Melting drives the primary differentiation of rocky planets into metallic core and silicate crust and mantle. Thermal models and measurements of the elemental and isotopic compositions of crust and mantle samples suggest that the inner solar system planets all experienced a magma ocean stage (30, 31). Molten metal and molten silicate are thought to (partially) equilibrate at the bottom of these oceans, leading to systematic depletions in siderophile element abundances in the rocky shells of Mercury, Earth, the Moon, and Mars (11, 32–34).

Equilibration between globally distributed magma and the overlying atmosphere, accompanied by significant outgassing from the convecting magma, can fundamentally alter the thickness and composition of the initial atmospheres that may have been inherited from the disk stage of a growing exoplanetary system (35, 36). The extent of melting of a rocky exoplanet during its magma ocean stage is determined by a combination of a planet's temperature profile and the solidus (temperature below which no liquid is present) and liquidus (temperature above which only liquid is present) of the rocks constituting the planet's outer silicate reservoir (35–37).

In current studies of rocky (exo)planet evolution, the melting behavior of planetary mantles is usually parametrized using experimental data on the melting of peridotitic or pyrolytic bulk compositions representing Earth's mantle (38–42). As reviewed in Hirschmann (38), it has been recognized that bulk compositional differences, in terms of cation ratios such as Mg/Fe or the total abundance of alkali metals, can affect melting temperatures. Such effects have also been observed in studies of solidus temperature variations for Martian mantle compositions (43). It is similarly well established that addition of volatile compounds such as water or CO_2 can lower the solidus of mantle compositions significantly (44, 45), but the effect of fO_2 on melting of peridotitic or pyrolytic compositions is not constrained.

High-Temperature Experiments

Studies of the effect of fO_2 on magma oceans have, to date, been limited to quantifying the link between fO_2 variations and changes in the redox states of the major cation iron (13, 26, 46), or linked directly to models of gas speciation in atmospheres influenced by magma ocean outgassing (35, 36, 47). Variations in solidus and liquidus temperatures of cooling magma oceans have largely been assessed in terms of variations in volatile abundances (48, 49). In this study we provide experimental evidence for a direct effect of oxygen fugacity on rock melting properties, in the absence of valence state variations in iron and in the absence of volatiles.

In order to isolate a possible effect of refractory oxygen on rock melting, we conducted a series of melting experiments on a synthetic iron-free basalt composition (50) at 1 atm and fO_2 conditions (imposed by air or CO/CO_2 gas mixtures) that cover a large section of the range of conditions found in rocky bodies in our solar system. All experiments were performed at nominally anhydrous conditions. Details of starting material synthesis, experimental setup, and conditions of our 16 experiments are given in *Methods* and in *SI Appendix*.

Results

Results are summarized in Table 1 in terms of the phases present in the experiments and their proportions. Compositional data for all phases are presented in *SI Appendix*. A summary of the experimental results and backscatter electron (BSE) microscope images

Table 1. Summary of experimental results

Exp.	T (°C)	Duration (h)	logfO_2	Glass proportions (wt.%)	Mineral proportions (wt. %)				
					Ol	Opx	Cpx	Pl	Ru
FefreeIW6	1,280	24	CO–CO_2 (logfO_2 = −11.5)	100					
FefreeIW5	1,250	24	CO–CO_2 (logfO_2 = −11.5)	100					
FefreeIW7	1,230	40	CO–CO_2 (logfO_2 = −11.5)	99		1			
FefreeIW4	1,200	36	CO–CO_2 (logfO_2 = −11.5)	36		8	16	40	
FefreeIW2	1,150	36	CO–CO_2 (logfO_2 = −11.5)	18		8	27	46.5	0.5
FefreeIW1	1,100	36	CO–CO_2 (logfO_2 = −11.5)	13			30	56	1
Fefree-7_3	1,230	40	CO–CO_2 (logfO_2 = −7)	100					
Fefree-7_1	1,200	36	CO–CO_2 (logfO_2 = −7)	58		6	15	21	
Fefree-7_2	1,150	36	CO–CO_2 (logfO_2 = −7)	29		8	20	43	
Fefree3	1,160	36	In air (logfO_2 = −0.7)	100					
Fefree4	1,140	36	In air (logfO_2 = −0.7)	100					
Fefree15	1,130	36	In air (logfO_2 = −0.7)	73	1		8	18	
Fefree5	1,100	36	In air (logfO_2 = −0.7)	44		6	15	35	
Fefree7	1,090	36	In air (logfO_2 = −0.7)	43		7	16	34	
Fefree8	1,050	36	In air (logfO_2 = −0.7)	27		7	22	44	
Fefree9	1,000	36	In air (logfO_2 = −0.7)	15		11	23	50	1

P = 1 atm for all experiments (Exp.). Mineral abbreviations: Ol, olivine; Opx, orthopyroxene; Cpx, clinopyroxene; Pl, plagioclase; Ru, rutile.

of representative polished run products are shown in Fig. 1. Our experiments indicate that oxygen fugacity significantly affects the liquidus temperature, the subliquidus melt percentages at a given temperature, and the appearance of mineral phases. At logfO_2 = −11.5 (close to the iron–wüstite buffer) and 1,100 °C, the composition contains 13 wt.% melt, coexisting with a mineral assemblage of clinopyroxene, plagioclase, and rutile. The melt percentage increases to 18 wt.% at 1,150 °C, and the phase assemblage becomes orthopyroxene + clinopyroxene + plagioclase + rutile + melt. Rutile is not present any more at 1,200 °C when the melt percentage has increased to 36 wt.%, and clinopyroxene and plagioclase melt out between 1,200 °C and 1,230 °C (when the melt percentage reaches 99 wt.%). Orthopyroxene disappears as the last phase between 1,230 and 1,250 °C, which constrains the liquidus temperature to 1,240 ± 10 °C.

The liquidus is significantly lower at the more oxygenated condition (logfO_2 = −0.7, in air). At this higher oxygen fugacity, 15 wt.% melt is present at 1,000 °C, coexisting with orthopyroxene + clinopyroxene + plagioclase + rutile. With the temperature increasing, rutile disappears at 1,050 °C (27 wt.% melt), and olivine replaces orthopyroxene at 1,130 °C (73 wt.% melt). The composition is fully molten at 1,140 °C, constraining the liquidus to 1,135 ± 5 °C.

At 1 atm and the intermediate logfO_2 = −7 and 1,150 °C, 29 wt.% of the composition is molten, in equilibrium with the mineral assemblage orthopyroxene + clinopyroxene + plagioclase. At 1,200 °C, the corresponding percentage of melt is 58 wt.%, and the sample is fully molten at 1,230 °C. The liquidus temperature is less well constrained at this fO_2, but, based on the increase in subliquidus melt percentages with increasing temperature, is estimated to be 1,215 ± 15 °C.

The temperature interval between solidus and liquidus, and the minerals coexisting with melt, are similar to observations in an experimental study of the 1-atm melting behavior of natural, iron-bearing terrestrial basalt (51). At a log fO_2 of ∼−11, the solidus of this natural composition is ∼1,080 °C, and the liquidus is ∼1,200 °C, with clinopyroxene, plagioclase, and olivine coexisting with melt until the late disappearance of clinopyroxene just below the liquidus.

In summary, our data indicate that the liquidus of iron-free basalt is lowered by 105 ± 10 °C when log fO_2 is increased by 11 log units. As indicated by dashed lines in Fig. 1, the effect is not linear, and is not restricted to the liquidus. Curves indicating constant melt weight percentages are subparallel to the liquidus temperature trend: Temperatures needed to achieve identical melt weight percentages down to at least 15 remain around 110 °C lower in oxidized conditions than in reduced conditions. Because of our choice of starting material composition, these significant variations in melting behavior cannot be ascribed to variations in cation behavior. In the absence of iron, the only cation that can realistically exhibit multiple valence states would be titanium. However, virtually all Ti in our experiments is expected to be Ti^{4+}. Trivalent titanium levels only become significant at conditions more reducing than in our most reduced experiments, and at temperatures much higher than the maximum temperatures achieved here (52). Volatile abundance variations can also be excluded. The maximum C level in our experiments is only ∼0.5 ppm based on its solubility in basaltic silicate melt at 1 atm (53). We conclude that refractory oxygen itself must cause the observed trends.

The abundance of refractory oxygen in silicate magma cannot be measured accurately; its abundance is commonly derived indirectly from measurements of cation abundances, where two oxygens are assigned to each Si atom, one to each Fe^{2+} atom, etc. This may have contributed to the lack of previous observations of the effect we observe. Recently, Fabbrizio et al. (54), in a study of the effect of fO_2 on europium partitioning between silicate minerals and melt, noted that melt percentages increased

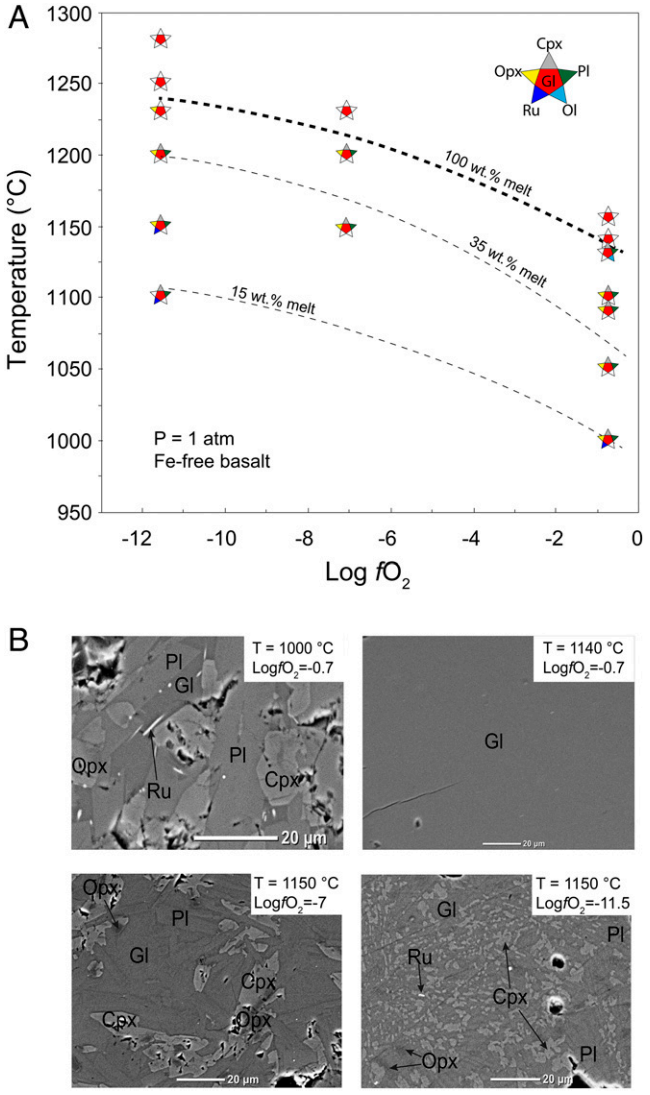

Fig. 1. (*A*) Liquidus and phase relations of Fe-free basalt as a function of oxygen fugacity at 1 atm. The bold dashed curve shows the approximate location of the liquidus as a function of fO_2. (*B*) Representative BSE images of experimental products illustrating the phases present at different conditions. The experimental conditions are shown in the top right of each BSE image. Abbreviations of phases: Ol, olivine; Opx, orthopyroxene; Cpx, clinopyroxene; Pl, plagioclase; Ru, rutile; Gl, silicate glass (liquid at high-temperature conditions).

as a function of increasing fO_2 at constant temperature in their iron-free system, but, as this was not the focus of their study, they did not expand on this observation. We suspect similar observations may have gone unnoticed in other experimental studies. Our results could also shed light on observations of variations in the chemical composition of natural(iron-bearing) mid-ocean ridge basalt (MORB) on Earth as a function of fO_2. Cottrell and Kelley (55) measured a decrease of incompatible trace element abundances with increasing fO_2. This is consistent with increased melt percentages at constant temperature as a function of increasing fO_2.

Conceptual Model and Implications

Conceptually, the hypothesis that refractory oxygen abundance variations strongly affect melting behavior requires the assumption that oxygen behaves like an incompatible element in systems containing minerals and silicate melt. Increasing its abundance in

a bulk composition at high fO_2 conditions leads to a lowering of the activities of the other (cation-bearing) components in silicate melt, leading to enhanced stability of melt with respect to coexisting minerals. We hypothesize that refractory oxygen incorporation into silicate melt occurs through depolymerization of the melt, similar to existing models of melt depolymerization due to the addition of H_2O (56–60).

In iron-bearing systems, the effects of oxygen fugacity on melting could be at least as large as in the iron-free system. At oxidizing conditions, trivalent iron (which is also an incompatible element) is more abundant than compatible divalent iron, leading to further enhanced melt stability. At reducing conditions, iron metal becomes stable. Metal segregation lowers the iron content of the silicate, which, in itself, is expected to further increase solidus and liquidus temperatures, on top of any increases that can be attributed to oxygen.

The cartoon in Fig. 2 illustrates the implications of our finding for the early evolution of rocky exoplanets, by comparing, qualitatively, the structure of two planets with the same relative cation abundances and thermal structure but different refractory oxygen content. In addition to the well-known effect of refractory oxygen content on relative core size (5, 61), our data suggest that higher refractory oxygen abundances cause more extensive melting in the interior. On the one hand, this corresponds to a deeper magma ocean for a given temperature profile, assuming the effect we observe in Fig. 1 down to ∼15 wt.% melt extends down to solidus temperatures and persists at higher pressure. On the other hand, lower liquidus temperatures at higher refractory oxygen abundances imply the magma ocean stage of planetary evolution will extend for longer periods of time. The latter effect may be further strengthened by the fact that deeper magma oceans would lead to more substantial degassing of volatiles from the planetary interior, forming a thicker atmosphere that provides better insulation against planetary cooling. Finally, this thicker atmosphere is likely to be dominated by more-oxidized species given the comparatively high fO_2 of the underlying mantle (47). If the planets contain significant amounts of hydrogen and carbon in their interiors, the main atmospheric constituents produced by outgassing of magma ocean would be H_2, CO, and CH_4 at reduced conditions, versus O_2, H_2O, and CO_2 at oxidized conditions.

Our dataset is insufficient at present to develop quantitative models of fO_2-controlled melting and crystallization in exoplanets, but, in principle, with additional experimental data, it should become feasible to better constrain the interior structure of rocky exoplanets based on mass-radius atmospheric composition considerations, including planetary fO_2 as an explicit variable. Because of the link between interior fO_2, magmatism, and extent and duration of planetary outgassing in the magma ocean stage, a coupling with future observations of rocky exoplanet atmospheric compositions and thicknesses may also be achievable.

Methods

Starting Materials. A synthetic Fe-free basalt based on an MORB composition from Melson et al. (50) was used as the starting compositions for our experiments. Following the methods described by Lin et al. (48), all experiments were performed under nominally anhydrous conditions.

The Fe-free basalt starting material was prepared by mixing appropriate proportions of high-purity (99.5 to 99.99%, Alfa Aesar) finely powdered oxides (SiO_2, TiO_2, Al_2O_3, and MgO) and carbonates ($CaCO_3$, Na_2CO_3, and K_2CO_3). The oxides SiO_2, TiO_2, Al_2O_3, and MgO were fired overnight at 1,100 °C, and $CaCO_3$, Na_2CO_3, and K_2CO_3 were stored at 110 °C overnight before use. The resulting starting material was homogenized under ethanol in an agate mortar for 1 h, dried in a fume hood, and subsequently decarbonated in an iron-free Pt crucible using a box furnace, by increasing temperature from 650 °C to 1,000 °C over 7 h. The CO_2-free mixture was then melted for 25 min at 1,550 °C to ensure full chemical homogenization. The melt was quenched rapidly by immersing the bottom of the Pt crucible in water.

Accurate knowledge of the starting material composition enhances the accuracy of mass balance calculations performed subsequently for each experimental run product. To this end, a shard of the starting material glass was mounted in epoxy, ground, polished, and carbon coated for chemical analysis. All remaining glass was crushed into powder in an agate ball mill for 90 min, and then stored at 110 °C for at least 24 h prior to use in the high-temperature experiments.

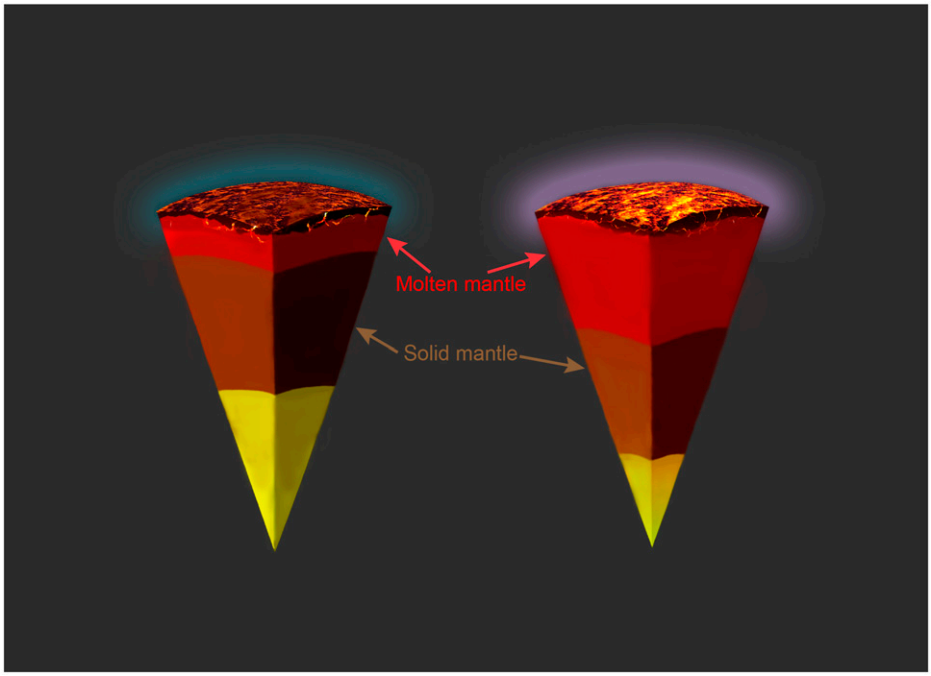

Fig. 2. Cartoon illustrating the structure of rocky exoplanets with identical relative cation abundances and thermal profiles at low (Left) and high (Right) planetary oxygen fugacity during their magma ocean stage. Oxidized planets have smaller metal cores (yellow), deeper magma oceans (red), and thicker, more oxidized atmospheres (purple). Solid lower mantles shown in claret.

The 1-atm High-Temperature Experiments. Three series of high-temperature, 1-atm experiments on the Fe-free starting composition were designed to run in oxidized (high fO_2) and reduced (low fO_2) conditions. Sample capsules were used instead of wires or foils, in order to maximize sample volumes. A Linn high-temperature box furnace using an ambient air atmosphere was used to achieve oxidized conditions, with temperatures calibrated against noble metal melting points. The oxygen partial pressure of air is assumed to be constant during the experiment, imposing a $\log fO_2$ of −0.7 on the samples.

Two-millimeter outer diameter (OD) Pt capsules with one end welded shut were loaded with compacted starting material. The starting material was first fully melted at 1,200 °C for 30 min, after which the temperature was slowly decreased to the target temperature with a ramp of 5 °C/h to promote crystal growth. Each experiment was then kept at the final target temperature for 36 h to ensure chemical equilibrium between all coexisting phases.

A Gero 1-atm gas-mixing furnace at Vrije Universiteit Amsterdam was used to perform the reduced experiments, using 2-mm OD Pt capsules. The oxygen fugacity of these experiments was controlled using a CO/CO_2 gas mixture, apportioned according to the *P-T-*fO_2 table in Deines et al. (62). The oxygen fugacity was verified using an yttria-stabilized ZrO_2 solid electrolyte sensor. Temperature was monitored with a $Pt_{70}Rh_{30}$–$Pt_{94}Rh_6$ (type B) thermocouple, and calibrated against noble metal melting points before the experiments. The experiment with target temperatures lower than 1,250 °C started by fully melting the charges at 1,250 °C for 30 min, then gradually reducing the temperature to the target temperature at a rate of 5 °C/h. The dwell duration at the target temperature varied between 36 and 40 h (Table 1). The two hottest experiments (1,250 °C and 1,280 °C) were run for 24 h.

Analytical Techniques. Experimental run products were mounted in epoxy, polished, and carbon coated for BSE imagery to assess the texture and mineralogy, and for quantitative compositional measurements using a scanning electron microscope (SEM). The chemical composition of the run product phases (minerals and melts) was determined using energy-dispersive spectrometry (EDS) measurements on a JEOL JCM-6000 Secondary Electron Microscope at Vrije Universiteit Amsterdam. Analyses were performed at an accelerating voltage of 15 kV with a focused spot (diameter of <1 μm) and 3-nA beam current, measured by an absorbed current meter attached to the sample stage, for a duration of 30 s. The analyses were performed standardless, with starting material glass and run product analyses performed in the same analytical session. Mineral and melt proportions were determined by mass balance calculations using the EDS data, and are reported in full in *SI Appendix*.

Data Availability. All study data are included in the article and *SI Appendix*.

ACKNOWLEDGMENTS. We thank J. Jing and M. Verburg for experimental assistance and technical assistance on SEM analyses and B. de Jong, K. Hakim, E. Kite, and J. Hernlund for constructive discussions. This research was supported by the National Science Foundation of China (Grants U1530402 and U1930401) to Center for High Pressure Science and Technology Advanced Research. W.v.W. acknowledges financial support from the Dutch Research Council Planetary and Exoplanetary Science program.

1. T. Lyubetskaya, J. Korenaga, Chemical composition of Earth's primitive mantle and its variance: 1. Method and results. *J. Geophys. Res.* **112**, B03211 (2007).
2. B. Fegley Jr., "Venus" in *Treatise on Geochemistry*, H. D. Holland, K. K. Turekian, Eds. (Elsevier Science, 2004), **vol. 1**, pp. 487–507.
3. L. R. Nittler, L. N. Chabot, T. L. Grove, P. N. Peplowski, "The chemical composition of mercury", in *Mercury: The View After MESSENGER*, S. C. Solomon, L. R. Nittler, B. J. Anderson, Eds. (Cambridge University Press, Cambridge, UK, 2018), pp. 30–51.
4. K. Lodders, B. Fegley Jr., An oxygen isotope model for the composition of Mars. *Icarus* **126**, 373–394 (1997).
5. C. T. Unterborn, W. R. Panero, The effects of Mg/Si on the exoplanetary refractory oxygen budget. *Astrophys. J.* **845**, 61 (2017).
6. D. J. Frost, C. A. McCammon, The redox state of Earth's mantle. *Annu. Rev. Earth Planet. Sci.* **36**, 389–420 (2008).
7. C. K. Shearer, J. J. Papike, J. M. Karner, Pyroxene europium valence oxybarometer: Effects of pyroxene composition, melt composition, and crystallization kinetics. *Am. Mineral.* **91**, 1565–1573 (2006).
8. C. Cartier, B. J. Wood, The role of reducing conditions in building Mercury. *Elements* **15**, 39–45 (2019).
9. K. Righter, H. Yang, G. Costin, R. T. Downs, Oxygen fugacity in the Martian mantle controlled by carbon: New constraints from the nakhlite MIL 03346. *Meteorit. Planet. Sci.* **43**, 1709–1723 (2008).
10. J. Wade, B. J. Wood, Core formation and the oxidation state of the Earth. *Earth Planet. Sci. Lett.* **236**, 78–95 (2005).
11. D. C. Rubie *et al.*, Accretion and differentiation of the terrestrial planets with implications for the compositions of early-formed Solar System bodies and accretion of water. *Icarus* **248**, 89–108 (2015).
12. D. J. Frost *et al.*, Experimental evidence for the existence of iron-rich metal in the Earth's lower mantle. *Nature* **428**, 409–412 (2004).
13. K. Armstrong, D. J. Frost, C. A. McCammon, D. C. Rubie, T. Boffa Ballaran, Deep magma ocean formation set the oxidation state of Earth's mantle. *Science* **365**, 903–906 (2019).
14. J. Deng, Z. Du, B. B. Karki, D. B. Ghosh, K. K. M. Lee, A magma ocean origin to divergent redox evolutions of rocky planetary bodies and early atmospheres. *Nat. Commun.* **11**, 2007 (2020).
15. J. F. Otegi, F. Bouchy, R. Helled, Revisited mass-radius relations for exoplanets below 120 M⊕. *Astron. Astrophys.* **634**, A43 (2020).
16. C. Dorn, J. H. Harrison, A. Bonsor, T. O. Hands, A new class of Super-Earths formed from high-temperature condensates: HD219134 b, 55 Cnc e, WASP-47 e. *Mon. Not. R. Astron. Soc.* **484**, 712–727 (2019).
17. A. Léger *et al.*, A new family of planets? "Ocean-Planets." *Icarus* **169**, 499–504 (2004).
18. L. T. Elkins-Tanton, S. Seager, Coreless terrestrial exoplanets. *Astrophys. J.* **688**, 628–635 (2008).
19. J. Moriarty, N. Madhusudhan, D. Fischer, Chemistry in an evolving protoplanetary disk: Effects on terrestrial planet composition. *Astrophys. J.* **787**, 81 (2014).
20. K. Hakim, A. van den Berg, A. Vazan, D. Höning, W. van Westrenen, C. Dominik, Thermal evolution of rocky exoplanets with a graphite outer shell. *Astron. Astrophys.* **630**, A152 (2019).
21. A. E. Doyle, E. D. Young, B. Klein, B. Zuckerman, H. E. Schlichting, Oxygen fugacities of extrasolar rocks: Evidence for an Earth-like geochemistry of exoplanets. *Science* **366**, 356–359 (2019).
22. A. E. Doyle, B. Klein, H. E. Schlichting, E. D. Young, Where are the extrasolar Mercuries? *Astrophys. J.* **901**, 10 (2020).
23. K. D. Putirka, J. C. Rarick, The composition and mineralogy of rocky exoplanets: A survey of >4000 stars from the Hypatia Catalog. *Am. Mineral.* **104**, 817–829 (2019).
24. J. W. Keefner, S. J. Mackwell, D. L. Kohlstedt, F. Heidelbach, Dependence of dislocation creep of dunite on oxygen fugacity: Implications for viscosity variations in Earth's mantle. *J. Geophys. Res.* **116**, B05201 (2011).
25. M. M. Hirschmann, Magma ocean influence on early atmosphere mass and composition. *Earth Planet. Sci. Lett.* **341–344**, 48–57 (2012).
26. P. A. Sossi *et al.*, Redox state of Earth's magma ocean and its Venus-like early atmosphere. *Sci. Adv.* **6**, eabd1387 (2020).
27. K. J. Zahnle, R. Lupu, D. C. Catling, N. Wogan, Creation and evolution of impact-generated reduced atmospheres of early Earth. *Planet. Sci. J.* **1**, 1–21 (2020).
28. F. Gaillard *et al.*, The diverse planetary ingassing/outgassing paths produced over billions of years of magmatic activity. *Space Sci. Rev.* **217**, 22 (2021).
29. J. L. Bada, How life began on Earth: A status report. *Earth Planet. Sci. Lett.* **226**, 1–15 (2004).
30. V. S. Solomatov, "Fluid dynamics of a terrestrial magma ocean" in *Origin of the Earth and Moon*, R. M. Canup, K. Righter, Eds. (University of Arizona Press, Tucson, AZ, 2000), pp. 323–338.
31. L. T. Elkins-Tanton, Magma oceans in the inner solar system. *Annu. Rev. Earth Planet. Sci.* **40**, 113–139 (2012).
32. N. Rai, W. van Westrenen, Core-mantle differentiation in Mars. *J. Geophys. Res. Planets* **118**, 1195–1203 (2013).
33. K. E. Vander Kaaden, F. M. McCubbin, Exotic crust formation on Mercury: Consequences of a shallow, FeO-poor mantle. *J. Geophys. Res. Planets* **120**, 195–209 (2015).
34. E. S. Steenstra *et al.*, Metal-silicate partitioning systematics of siderophile elements at reducing conditions: A new experimental database. *Icarus* **335**, 113391 (2020).
35. E. S. Kite, M. N. Barnett, Exoplanet secondary atmosphere loss and revival. *Proc. Natl. Acad. Sci. U.S.A.* **117**, 18264–18271 (2020).
36. E. S. Kite, L. Schaefer, Water on hot rocky exoplanets. *Astrophys. J. Lett.* **909**, L22 (2021).
37. R. J. Spaargaren, M. D. Ballmer, D. J. Bower, C. Dorn, P. J. Tackley, The influence of bulk composition on the long-term interior-atmosphere evolution of terrestrial exoplanets. *Astron. Astrophys.* **643**, A44 (2020).
38. M. M. Hirschmann, Mantle solidus: Experimental constraints and the effects of peridotite composition. *Geochem. Geophys. Geosyst.* **1**, 2000GC000070 (2000).
39. G. Fiquet *et al.*, Melting of peridotite to 140 gigapascals. *Science* **329**, 1516–1518 (2010).
40. D. Andrault *et al.*, Solidus and liquidus profiles of chondritic mantle: Implication for melting of the Earth across its history. *Earth Planet. Sci. Lett.* **304**, 251–259 (2011).
41. D. Andrault, Deep and persistent melt layer in the Archaean mantle. *Nat. Geosci.* **11**, 139–143 (2018).
42. Y. Miyazaki, J. Korenaga, On the timescale of magma ocean solidification and its chemical consequences: 1. Thermodynamic database for liquid at high pressures. *J. Geophys. Res.* **124**, 3382–3398 (2019).
43. S. Ding, R. Dasgupta, K. Tsuno, The solidus and melt productivity of nominally anhydrous Martian mantle constrained by new high pressure-temperature experiments—Implications for crustal production and mantle source evolution. *J. Geophys. Res. Planets* **123**, e2019JE006078 (2020).

44. I. Kushiro, The system forsterite-diopside-silica with and without water at high pressures. *Am. J. Sci.* **267A**, 269–294 (1969).
45. R. Dasgupta, M. M. Hirschmann, Melting in the Earth's deep upper mantle caused by carbon dioxide. *Nature* **440**, 659–662 (2006).
46. S. Berthet, V. Malavergne, K. Righter, Melting of the Indarch meteorite (EH4 chondrite) at 1 GPa and variable oxygen fugacity: Implications for early planetary differentiation processes. *Geochim. Cosmochim. Acta* **73**, 6402–6420 (2009).
47. L. Schaefer, B. Fegley Jr., Redox states of initial atmospheres outgassed on rocky planets and planetesimals. *Astrophys. J.* **843**, 120 (2017).
48. Y. Lin, E. J. Tronche, E. S. Steenstra, W. van Westrenen, Evidence for an early wet Moon from experimental crystallization of the lunar magma ocean. *Nat. Geosci.* **10**, 14–18 (2017).
49. Y. Lin, H. Hui, X. Xiao, S. Shang, W. van Westrenen, Experimental constraints on the solidification of a hydrous lunar magma ocean. *Meteorit. Planet. Sci.* **55**, 207–230 (2020).
50. W. G. Melson, T. L. Vallier, T. L. Wright, G. Byerly, J. Nelen, Chemical diversity of abyssal volcanic glass erupted along Pacific, Atlantic, and Indian Ocean sea-floor spreading centers. *Geophys. Pac. Ocean Basin Margin* **19**, 351–368 (1976).
51. L. H. Cohen, K. Ito, G. C. Kennedy, Melting and phase relations in an anhydrous basalt to 40 kilobars. *Am. J. Sci.* **265**, 475–518 (1967).
52. A. A. Borisov, The Ti^{4+}/Ti^{3+} ratio of magmatic melts: Application to the problem of the reduction of lunar basalts. *Petrology* **20**, 391–398 (2012).
53. J. E. Dixon, E. M. Stolper, J. R. Holloway, An experimental study of water and carbon dioxide solubilities in Mid-ocean ridge basaltic liquids. Part I: Calibration and solubility models. *J. Petrol.* **36**, 1607–1631 (1995).
54. A. Fabbrizio, M. W. Schmidt, M. Petrelli, Effect of fO_2 on Eu partitioning between clinopyroxene, orthopyroxene and basaltic melt: Development of a Eu^{3+}/Eu^{2+} oxybarometer. *Chem. Geol.* **559**, 119967 (2021).
55. E. Cottrell, K. A. Kelley, Redox heterogeneity in mid-ocean ridge basalts as a function of mantle source. *Science* **340**, 1314–1317 (2013).
56. Y. Lin, W. van Westrenen, Oxygen as a catalyst in the Earth's interior? *Natl. Sci. Rev.* **8**, nwab009 (2021).
57. T. W. Sisson, T. L. Grove, Experimental investigations of the role of H_2O in calc-alkaline differentiation and subduction zone magmatism. *Contrib. Mineral. Petrol.* **113**, 143–166 (1993).
58. T. Grove, N. Chatterjee, S. Parman, E. Medard, The influence of H_2O on mantle wedge melting. *Earth Planet. Sci. Lett.* **249**, 74–89 (2006).
59. L. Hong *et al.*, Oxidized Late Mesozoic subcontinental lithospheric mantle beneath the eastern North China Craton: A clue to understanding cratonic destruction. *Gondwana Res.* **81**, 230–239 (2020).
60. X. Xue, M. Kanzaki, Dissolution mechanisms of water in depolymerized silicate melts: Constraints from ^{1}H and ^{29}Si NMR spectroscopy and ab initio calculations. *Geochim. Cosmochim. Acta* **68**, 5027–5057 (2004).
61. R. G. Trønnes *et al.*, Core formation, mantle differentiation and core-mantle interaction within Earth and the terrestrial planets. *Tectonophysics* **760**, 165–198 (2019).
62. P. Deines, R. H. Nafziger, G. C. Ulmer, E. Woermann, Temperature-oxygen fugacity tables for selected gas mixtures in the system C–H–O at one atmosphere total pressure. *Metall. Mater. Trans. B Process Metall. Mater. Proc. Sci.* **7**, 143 (1976).